

# Controlled Crystal Plane Orientations in the ZnO Transport Layer Enable High-Responsivity, Low-Dark-Current Infrared Photodetectors

Darshan H. Parmar, Joao M. Pina, Tong Zhu, Maral Vafaie, Ozan Atan, Margherita Biondi, Amin M. Najjariyan, Sjoerd Hoogland, and Edward H. Sargent\*

Colloidal quantum dots (CQD) have emerged as attractive materials for infrared (IR) photodetector (PD) applications because of their tunable bandgaps and facile processing. Presently, zinc oxide is the electron-transport layer (ETL) of choice in CQD PDs; however, ZnO relies on continuous ultraviolet (UV) illumination to remove adsorbed oxygen and maintain high external quantum efficiency (EQE), speed, and photocurrent. Here, it is shown that ZnO is dominated by electropositive crystal planes which favor excessive oxygen adsorption, and that this leads to a high density of trap states, an undesired shift in band alignment, and consequent poor performance. Over prolonged operation without UV exposure, oxygen accumulates at the electropositive planes, trapping holes and degrading performance. This problem is addressed by developing an electroneutral plane composition at the ZnO surface, aided by atomic layer deposition (ALD) as the means of materials processing. It is found that ALD ZnO has 10× lower binding energy for oxygen than does conventionally deposited ZnO. IR CQD PDs made with this ETL do not require UV activation to maintain low dark current and high EQE.

## 1. Introduction

Infrared (IR) photodetectors (PDs) are used in machine vision, optical communications, surveillance, biological sensing, and spectroscopy. Colloidal quantum dots (CQD) offer size-tunable bandgap, solution processing, and high optical absorption in the IR.<sup>[1–4]</sup> Much literature on CQD PDs grows out of the extensive body of work on CQD solar cells. As such, many efficient PbS CQD PDs have adopted the prevalent solar cell heterojunction comprising a CQD active layer, a hole-transport layer (HTL), and a metal-oxide-based electron-transport layer (ETL). After early success as the ETL in PbS CQD solar cells, ZnO nanoparticles (NPs) have been widely adopted as the ETL of choice in CQD and organic PDs.<sup>[5–8]</sup> ZnO is attractive because of its

high electron mobility, n-type conductivity, wide bandgap (favoring hole-blocking), and suitable electron affinity.<sup>[9–12]</sup>

ZnO NPs have one significant disadvantage: they require continuous illumination by ultraviolet (UV) light in order to maintain performance.<sup>[13–16]</sup> In the absence of such UV activation, oxygen adsorbed at the ZnO NPs surface creates surface states into which carriers become trapped, hindering the extraction of photoelectrons through the ZnO NPs layer.<sup>[13–16]</sup> The oxygen can be removed using UV illumination; however, as IR PDs cannot be continuously irradiated with UV illumination, new ETLs that avoid oxygen adsorption need to be explored (Figure 1a).

The central purpose of this work is to investigate the origins of the UV activation problem in ZnO NPs. We find that ZnO NPs favor electropositive crystal planes. Since ALD is known to promote alternate


crystal planes,<sup>[17–19]</sup> we investigated this materials processing strategy instead and found that its planes are more electroneutral and have 10 times lower binding energy with oxygen than do the ZnO NP planes. We report, as a result, UV-activation-free ALD-based ETL devices with an improved external quantum efficiency (EQE), dark current, stability, and response time compared to prior CQD-based IR PDs.

## 2. Results and Discussion

UV activation of ZnO NPs is not permanent. UV-activated devices degrade in performance within minutes of removing the UV source. The output photocurrent from UV-activated ZnO NPs devices irradiated with 5 mW cm<sup>-2</sup> of broadband IR light was measured over time (Figure 1b). The photocurrent diminished in a matter of minutes. Another UV activation at 37 h yielded similar results with the photocurrent diminishing quickly. The EQE and device bandwidth are also lower without UV activation (Figures 1d,e).

To verify the need for UV light, we measured devices' photocurrent upon exposure to different parts of the solar spectrum (Figure 1c). The devices had an excitonic peak chosen for detection of 950 nm light; however, we saw a marked increase of photocurrent only when we illuminated it with <400 nm

D. H. Parmar, J. M. Pina, T. Zhu, M. Vafaie, O. Atan, M. Biondi, A. M. Najjariyan, S. Hoogland, E. H. Sargent  
The Edward S. Rogers Department of Electrical and Computer Engineering  
University of Toronto  
Toronto, Ontario M5S 3G4, Canada  
E-mail: ted.sargent@utoronto.ca

 The ORCID identification number(s) for the author(s) of this article can be found under <https://doi.org/10.1002/adma.202200321>.

DOI: 10.1002/adma.202200321

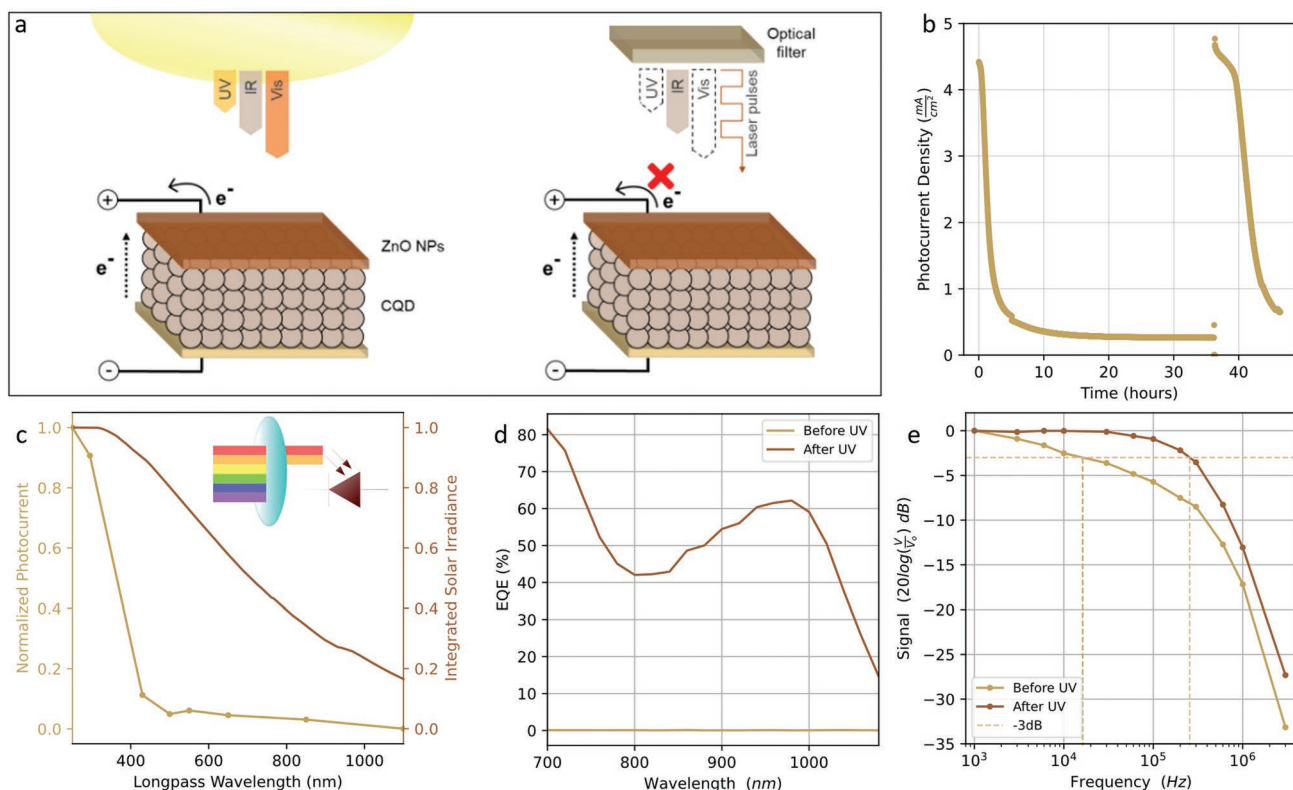


**Figure 1.** a) Schematic of solar cell and PD applications of the devices. Solar cells are continuously illuminated with UV wavelengths available in the solar spectrum. However, IR PDs use filters to remove non-IR wavelengths and rely on monochromatic IR sources. b) Photocurrent density of ZnO NP devices over time under constant IR illumination ( $5 \text{ mW cm}^{-2}$ ). Devices were UV activated at 0 h and again at 37 h. c) Normalized photocurrent (normalized to initial output current) from devices in response to illumination from various portions of the solar spectrum. The photocurrent increases when devices are illuminated with wavelengths  $< 400 \text{ nm}$ . d) EQE spectra of ZnO NP devices before and after UV activation showing dramatic increase in EQE after UV activation. e) Frequency bandwidth plots of ZnO NP device before and after UV activation. 3 dB cut-off frequencies are marked with crosshairs.

light—corresponding to the bandgap of ZnO. We thus assign a crucial role to photogenerated carriers in the ZnO in the UV activation phenomenon.

We studied further the origins of the need for UV activation. Literature reports that adsorbed oxygen causes surface traps in ZnO NPs, UV exposure removes the adsorbed oxygen, and the surface traps are thus quenched.<sup>[13–16]</sup> ZnO in NP and sol-gel forms favors different crystal planes than does ALD ZnO.<sup>[17–19]</sup> Since oxygen-binding requires Coulombic interaction with the surface, we posit that the crystal planes in ZnO NPs could be responsible for attracting oxygen to the ETL-CQD interface.

We looked at electrical characteristics for indicators of surface traps in the ETL, finding that non-activated devices (Before UV) have a smaller current density at forward bias compared to activated devices (After UV) (Figure 2a), agreeing with prior studies and their interpretation.<sup>[20–22]</sup> Intensity-dependent fall-time measurements can assess relative trap state densities within photodiodes.<sup>[23–25]</sup> Decreasing fall-times with increasing optical intensity are indicative of higher trap density (Figure S7, Supporting Information). In this experiment, we studied the fall time of devices (we report the fall time as the time for the photocurrent to drop from 90% of maximum to 10% of maximum) versus optical intensity. From Figure 2b we see that non-activated ZnO NP devices do show the signature decrease in fall-times with increasing optical intensity, whereas there is

no such correlation for activated ZnO NP devices. ALD devices were measured without UV activation, yet they showed no correlation of fall times with optical intensity.

We therefore explored the crystal planes possibility. Density functional theory (DFT) calculations (Figure 3) suggest that crystal planes with a high oxygen affinity also possess high defect densities. The photoluminescence (PL) spectrum of ZnO is related to defect density: it exhibits band edge emission at  $\approx 3.5 \text{ eV}$ , and defect emission due to oxygen vacancies at  $2\text{--}2.5 \text{ eV}$ .<sup>[13,26,27]</sup> Comparing the relative heights of the emission peak in Figure 2c, we find evidence that defective oxygen-attracting planes are more prominent in ZnO NPs compared to ALD ZnO. We also performed electrostatic force microscopy (EFM) measurements (Figure 2d). We find that NPs have a more heterogeneous electrostatic force profile than does the ALD surface, suggesting the possibility of diverse planes. This may also correspond to an increased possibility of electropositive planes.

To explore the crystal planes further, we conducted X-ray diffraction (XRD) measurements on ZnO NPs and ALD ZnO layers. We compare the relative peak heights of the XRD profiles of ZnO NPs and ALD ZnO to estimate, qualitatively, the relative prominence of the various crystal planes.<sup>[17–19]</sup> In Figure 3a,b, we find that (10–11) and (10–12) planes are more prominent in ZnO NPs than in ALD ZnO. ALD ZnO, by

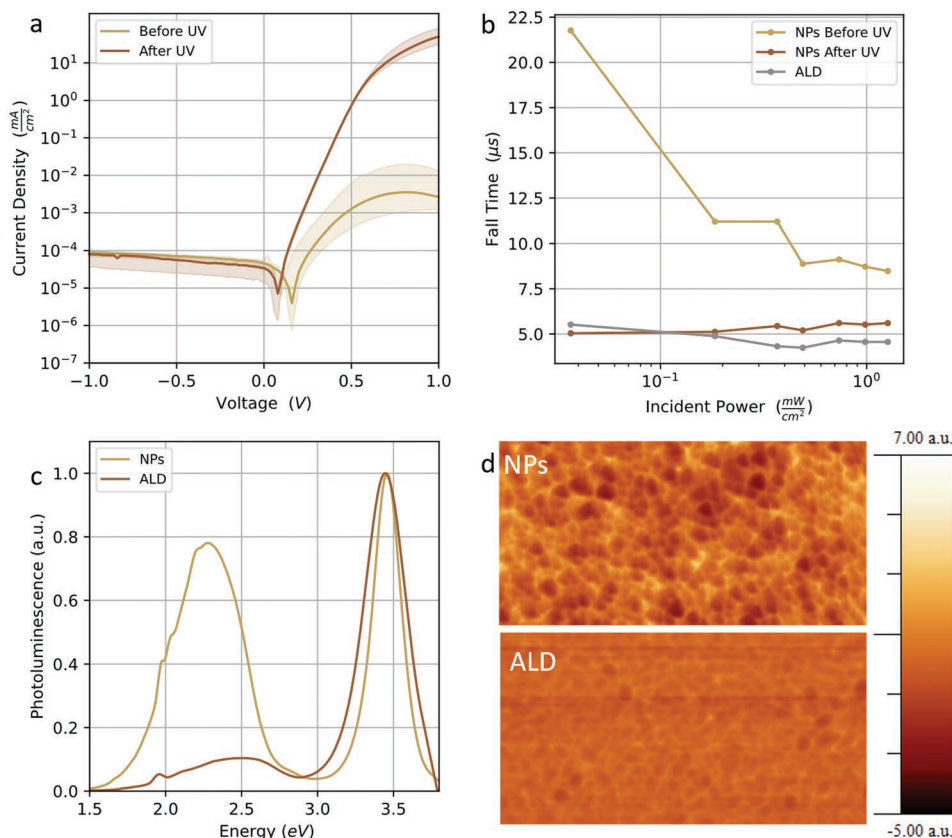


**Figure 2.** a) Current–voltage characteristic of ZnO NPs before and after UV activation. b) Fall times of ZnO NPs before and after UV activation, and ALD devices as a function of increasing incident optical power. c) PL spectra of NPs and ALD samples showing more prominent defect emission in NPs samples. d) EFM of ZnO NPs and ALD ZnO samples showing more heterogeneous surface for NPs.

contrast, favors (10–10) planes. We hypothesize that (10–11) and (10–12) planes are more electropositive, while (10–10) planes are expected to be neutral. This agrees with the idea that more electropositive planes in ZnO NPs attract oxygen more readily, while the neutral planes more prominent in ALD ZnO are less prone to oxygen adsorption so do not need UV activation.

DFT studies included evaluation of the binding energies of oxygen to (10–10), (10–11), and (10–12) planes, which we found to be  $-0.49$ ,  $-4.79$ , and  $-3.78$  eV respectively (Figure 3c). Further DFT calculations help us interpret XPS. Both (10–10) and (10–12) planes are unlikely to form oxygen vacancies because of their positive formation energies for this process. However, (10–11) is prone to oxygen vacancies with a corresponding formation energy of  $-3.38$  eV (Figure 3f). Oxygen defects, therefore, serve as a proxy to observing the prominence of (10–11) planes in ZnO, so we can corroborate the XRD peak analysis with X-ray photoelectron spectroscopy (XPS). The XPS spectrum of oxygen can be deconvoluted into three peaks, OI ( $\approx 530.0$  eV), OII ( $\approx 530.5$  eV), and OIII ( $\approx 532.0$  eV).<sup>[26]</sup> OI corresponds to oxygen ions in the regular ZnO lattice. OII derives from oxygen ions in close proximity to oxygen vacancies in the ZnO lattice as the absence of nearby oxygen ions increases the binding energy in the remaining oxygen ions. OIII is sensitive to sample preparation as it corresponds to species bound to the surface of the material such as ambient moisture. The greater amount of OII species in ZnO NPs compared to in ALD ZnO

agrees with the picture wherein the oxygen-philic (10–11) plane is more prominent in ZnO NPs than in ALD ZnO (Figure 3d,e).

We then further explored the improved fabrication of photodiodes using ALD ZnO as the ETL. We incorporated aluminum into the ALD ZnO layer (AZO) to improve further the EQE, since AZO narrows the bandgap and lowers the conduction band minimum.<sup>[14,28]</sup> ALD ZnO-only samples and AZO both showed the complete absence of a need for UV activation (Figure S4, Supporting Information); the AZO devices' EQE spectrum shows a well-defined excitonic peak at 950 nm with 70% EQE (Figure 4a). In Figure 4b, the current–voltage characteristics at various illumination intensities were measured at an excitation wavelength of 825 nm. We observe that rectifying behavior is maintained for all measured illumination powers, and that the open-circuit voltage increases with illumination. Figure 4c shows that the dynamic range of the ALD devices spans over 4 orders of magnitude. Photodetection speed was determined by measuring the transient photocurrent response for devices with a pixel area of  $0.2 \text{ mm}^2$  (Figure 4e). The inset shows the raw temporal signal of ALD AZO. A median fall-time of 210 ns was achieved with ALD AZO devices.

We evaluated the operating stability of devices for 100 h under continuous  $5 \text{ mW cm}^{-2}$  illumination. The devices retained 100% of the initial photocurrent under ambient air (Figure 4d). Figure 4f compares the ALD devices to prior PD literature at similar wavelengths.<sup>[6,7,29–34]</sup> The ALD devices

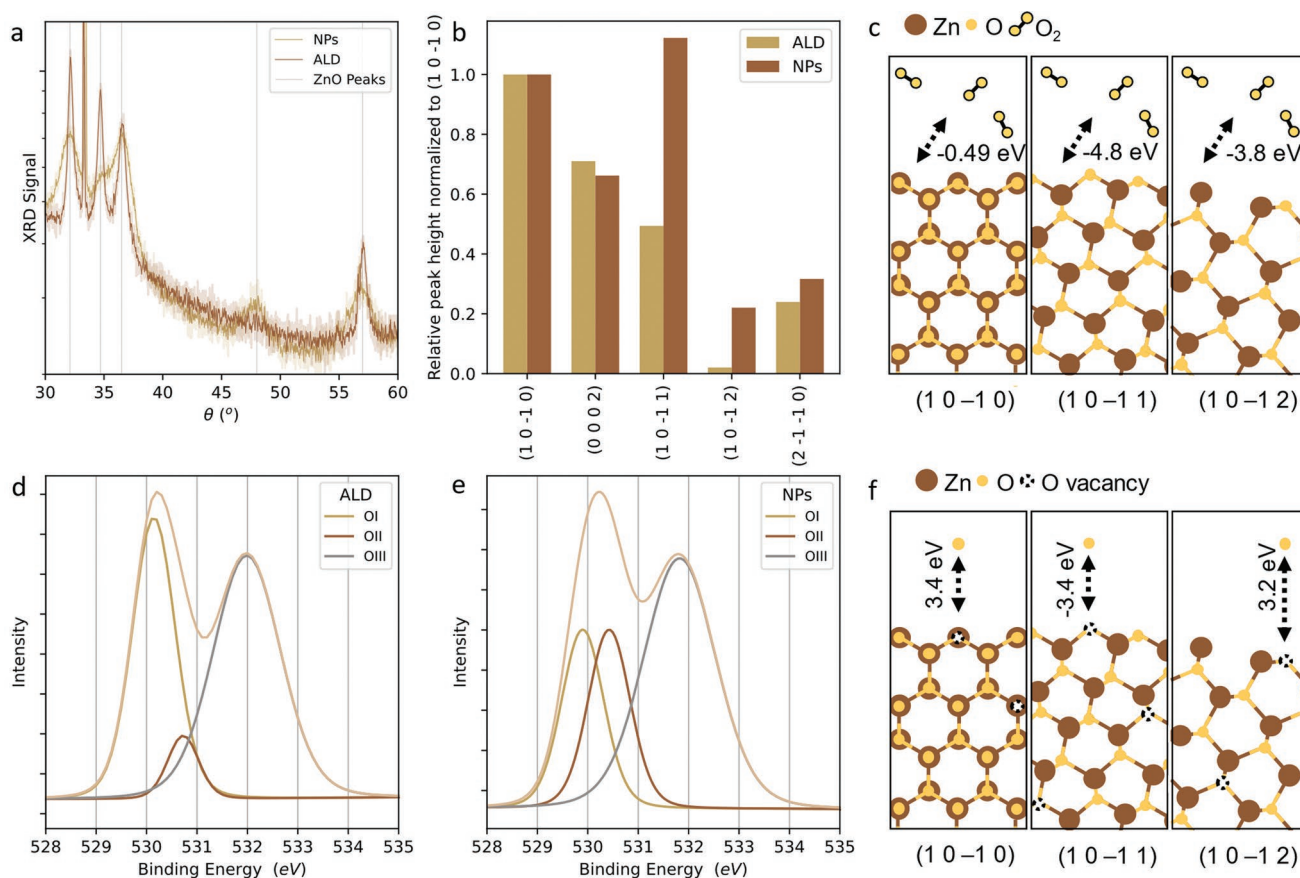


**Figure 3.** a) XRD of ZnO NPs and ALD ZnO with ZnO peaks marked with gray vertical lines. Background silicon peaks are visible as the samples were prepared on a silicon substrate. b) Relative XRD peak heights of the ZnO peaks normalized to (10-10) plane for ZnO NPs and ALD ZnO. c) Schematic showing DFT-calculated binding energy of oxygen to various ZnO plane orientations. d) XPS of ALD ZnO with envelope signal deconstructed into component oxygen peaks. e) XPS of ZnO NPs with envelope signal deconstructed into component oxygen peaks. f) Schematic showing DFT-calculated formation energy of oxygen vacancies in various ZnO plane orientations.

provide an improvement in EQE, dark current, speed (fall times), and stability compared to prior works.

### 3. Conclusion

This work establishes ALD ZnO as a practical improvement upon ZnO NPs as the ETL of choice in IR PDs. It will be of interest to explore whether some of these ideas can also be extended to longer wavelengths, such as in the SWIR. Unfavorable ZnO plane orientations are identified as the cause of oxygen adsorption to ZnO NPs, requiring repeatedly UV illumination. Since repeated UV illumination of IR PDs is not practical in most applications, ALD ZnO is demonstrated as an activation-free alternative. The optimized ALD ZnO devices significantly improve the EQE, dark current, and stability of IR PDs.

### 4. Experimental Section

**Synthesis and Exchange of PbS CQD:** Oleic-acid-capped CQD were synthesized using published methods.<sup>[35]</sup> The oleic acid ligands were exchanged for halide ligands and an ink was made for spin coating, all using a published exchange and ink synthesis method.<sup>[36]</sup>

**Indium Tin Oxide (ITO) Cleaning:** ITO glass substrates were cleaned in an ultrasonic bath of water, acetone, and isopropyl alcohol for 60, 30, and 30 min respectively. The substrates were fully dried before ETL deposition.

**ETL Deposition:** ZnO NPs were synthesized using a published method.<sup>[5]</sup> Two layers of ZnO NPs solution (100  $\mu$ L for each layer) were spin-coated on clean ITO at 5000 RPM for 30 s consecutively.

A Picosun R-200 was used for ALD. ITO substrates were heated at 150  $^{\circ}$ C for 10 min, and then treated with oxygen plasma for 10 min prior to ALD. The pre-treated substrates were then loaded into the pre-heated ALD chamber (150  $^{\circ}$ C), and the recipe below was used for deposition. The following precursors were used: diethylzinc (DEZ) (95% purity), and trimethylaluminum (TMA) (99.999% purity), both from Strem Chemicals, as well as distilled water. Following ALD, the samples were annealed at 300  $^{\circ}$ C on a hot plate for 30 min. The samples were allowed to cool before CQD layer deposition

- DEZ PULSE: 0.1 s
- DEZ PURGE: 5 s
- TMA PULSE: 0.1 s
- TMA PURGE: 5 s
- Water PULSE: 0.1 s
- Water PURGE: 6 s
- Carrier Gas: For DEZ and TMA lines: 150 sccm
- Carrier Gas for H<sub>2</sub>O line: 200 sccm
- Reactor flow (MFC 1) was at 300 sccm during deposition.



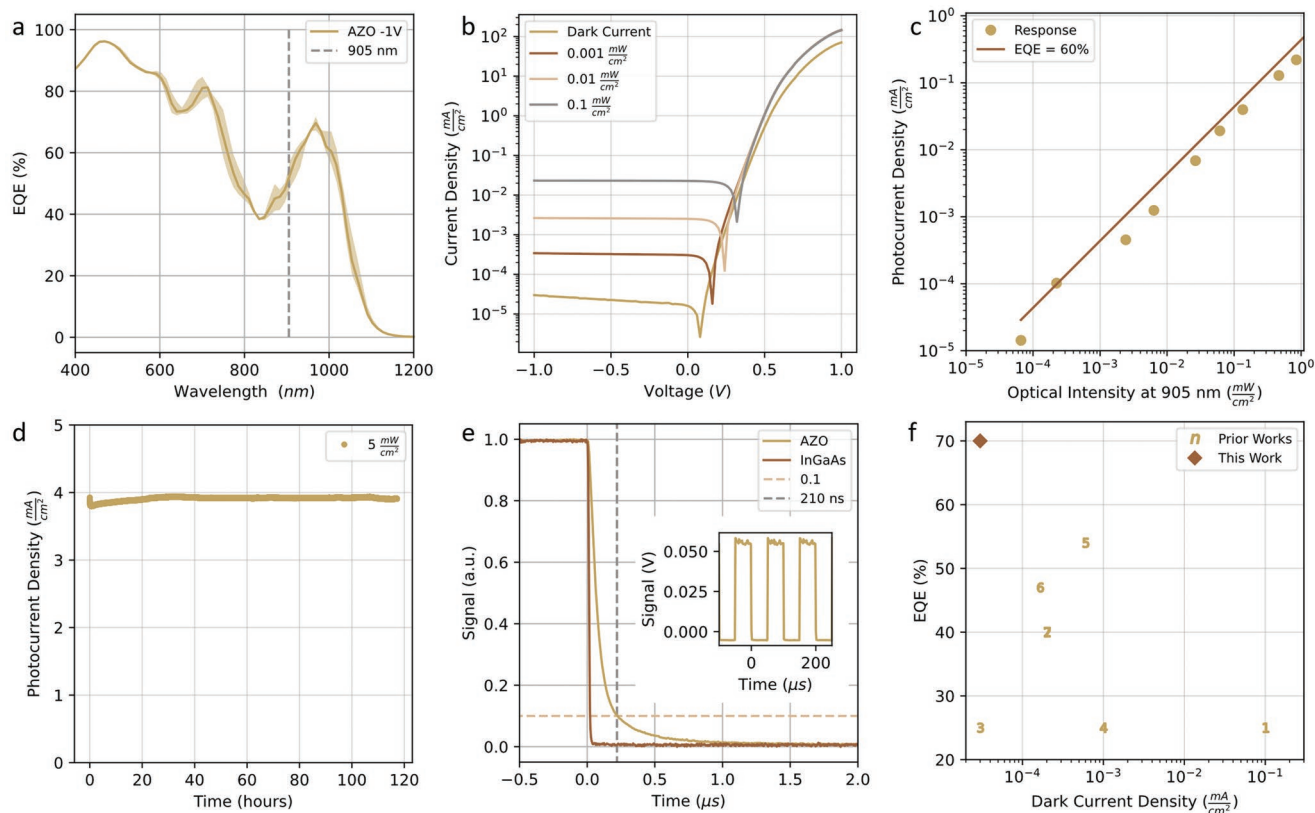


**Figure 4.** a) EQE spectrum of ALD AZO devices. b) Current–voltage characteristic of ALD AZO devices at various illumination intensities (illuminated with an 825 nm laser). c) Dynamic range measurement of ALD AZO devices. d) Photocurrent density of ALD AZO devices measured under continuous illumination. e) Temporal response of ALD AZO compared to commercial InGaAs photodiode with cursors showing fall time of 210 ns. Inset shows the raw temporal signal of ALD AZO. f) Comparison of current work with prior literature with regards to dark current density and EQE (see Figure S6, Supporting Information, for details).

**CQD Layer Deposition:** Using 50  $\mu\text{L}$  of CQD ink, the active layer was spin-coated onto the samples under a flow of nitrogen at 1500 to 2000 RPM for 60 s. The deposited films were annealed at 70  $^{\circ}\text{C}$  in a nitrogen-filled glovebox for 15 min.

**Hole-Transport Layer and Top Contact:** Layer-by-layer ligand exchange was used to deposit a 1,2-ethanedithiol (EDT)-PbS HTL. PbS CQD with an excitonic peak at 850 nm was used for the HTL. 47  $\mu\text{L}$  of oleic-acid-capped PbS CQD were deposited on top of the active layer at 2500 RPM for 10 s. Immediately afterwards, the layer was soaked in 0.01% EDT solution in 3:2 acetonitrile:ethyl acetate solvent for 30 s. The sample was spun again with the same parameters and 3:2 acetonitrile:ethyl acetate solvent solution without EDT was used to wash the sample 3 times. The whole process was repeated twice to deposit two layers. Finally, a 120 nm layer of gold was deposited as the top electrode using electron-beam evaporation.

**Characterization:** Details of the DFT calculations are provided in the Supporting Information. Current–voltage measurements were taken using a Keithley 2400 source meter. The photoresponse in non-activated ZnO NPs (Figure 1c) was measured as follows. Long-pass filters of increasingly shorter cut-off wavelengths were used to truncate the air mass 1.5 (AM 1.5G) illumination, and the resultant photocurrent in non-activated devices was measured. Since the detection wavelength of these devices was 950 nm, a peak was expected at that wavelength. However, below 950 nm there was only a marginal increase in the normalized photocurrent of the device which was even lower than the gradual increase in the integrated solar irradiance (a representation of the incident energy). For fall time measurements, and photocurrent measurements, an 825 nm laser modulated at 10 kHz with a 50% duty cycle was used to illuminate the pixel. EQE spectra were measured using a Newport

Quant-X 300 measurement system. For stability measurements (Figure 1b and Figure 4d), devices were encapsulated using epoxy in a nitrogen environment. They were then irradiated with a solar lamp truncated to 550–750 nm while the photocurrent at 0 V was measured using a Keithley 2400 source meter. XRD measurements were made using a Rigaku MiniFlex 600 powder X-ray diffractometer equipped with a NaI scintillation counter and using monochromatized Cu  $K\alpha$  radiation ( $\lambda = 0.15406$  nm). For PL measurements, ZnO samples were optically excited using a 330 nm femtosecond laser source with a repetition rate of 5 kHz. The laser source consisted of a Yb:KGW regenerative amplifier (Pharos, Light Conversion) with 1030 nm fundamental which was passed through an optical parametric amplifier (Orpheus, Light Conversion) to generate the 330 nm pump light pulse. The resultant spectra were collected in transmission mode with a UV–vis USB 2000+ spectrometer (Ocean Optics). AFM and EFM data were collected using an Asylum Research Cypher machine in the “Air AC Mode”. The data were analyzed using WSxM software.<sup>[37]</sup> XPS and UPS measurements were conducted at University of Alberta’s nanofAB facility using a Kratos AXIS Ultra machine.

**Statistical Analysis:** The data were used without any transformation with the exception of the following: Figures 1c, 2c, 3b, and 4e. Figure 1c was normalized to maximum photocurrent; Figure 2b was normalized to band edge emission (3.4 eV); Figure 3b was normalized relative to the (10–10) peak; Figure 4e was normalized to the maximum signal. At least four samples were used, and the median was plotted for all figures except: Figures 2b, 3d, 3e, and 4e where a single representative sample was used. In Figures 2a, 3a, and 4a, the bands surrounding the main curves correspond to the minimum and maximum values measured from all of the samples.

## Supporting Information

Supporting Information is available from the Wiley Online Library or from the author.

## Acknowledgements

D.H.P. and J.M.P. contributed equally to this work.

## Conflict of Interest

The authors declare no conflict of interest.

## Data Availability Statement

The data that support the findings of this study are available from the corresponding author upon reasonable request.

## Keywords

atomic layer deposition, colloidal quantum dots, crystal plane orientations, infrared photodetectors, ultraviolet activation

Received: January 11, 2022

Revised: February 21, 2022

Published online: March 20, 2022

- [1] S. A. McDonald, G. Konstantatos, S. Zhang, P. W. Cyr, E. J. D. Klem, L. Levina, E. H. Sargent, *Nat. Mater.* **2005**, *4*, 138.
- [2] O. E. Semonin, J. M. Luther, S. Choi, H. Y. Chen, J. Gao, A. J. Nozik, M. C. Beard, *Science* **2011**, *334*, 1530.
- [3] M. Yuan, M. Liu, E. H. Sargent, *Nat. Energy* **2016**, *1*, 16016.
- [4] M. Vafaie, J. Z. Fan, A. Morteza Najarian, O. Ouellette, L. K. Sagar, K. Bertens, B. Sun, F. P. García de Arquer, E. H. Sargent, *Matter* **2021**, *4*, 1042.
- [5] C. H. M. Chuang, P. R. Brown, V. Bulović, M. G. Bawendi, *Nat. Mater.* **2014**, *13*, 796.
- [6] J. R. Manders, T.-H. Lai, Y. An, W. Xu, J. Lee, D. Y. Kim, G. Bosman, F. So, *Adv. Funct. Mater.* **2014**, *24*, 7205.
- [7] R. Sliz, M. Lejay, J. Z. Fan, M. J. Choi, S. Kinge, S. Hoogland, T. Fabritius, F. P. García de Arquer, E. H. Sargent, *ACS Nano* **2019**, *13*, 11988.
- [8] M. Biondi, M. J. Choi, Z. Wang, M. Wei, S. Lee, H. Choubisa, L. K. Sagar, B. Sun, S. W. Baek, B. Chen, P. Todorović, A. M. Najarian, A. Sedighian Rasouli, D. H. Nam, M. Vafaie, Y. C. Li, K. Bertens, S. Hoogland, O. Voznyy, F. P. García de Arquer, E. H. Sargent, *Adv. Mater.* **2021**, *33*, 2101056.
- [9] C. Pacholski, A. Kornowski, H. Weller, *Angew. Chem., Int. Ed.* **2002**, *41*, 1188.
- [10] W. J. E. Beek, M. M. Wienk, M. Kemerink, X. Yang, R. A. J. Janssen, *J. Phys. Chem. B* **2005**, *109*, 9505.
- [11] H. Aqoma, A. Mubarak, W. T. Hadmojo, E.-H. Lee, T.-W. Kim, K. Ahn, S.-H. Oh, S.-Y. Jang, H. Aqoma, M. al Mubarak, W. T. S. Hadmojo, Y. Jang, E.-H. Lee, T.-W. Kim, T. K. Ahn, S.-H. Oh, *Adv. Mater.* **2017**, *29*, 1605756.
- [12] M. Liu, O. Voznyy, R. Sabatini, F. P. García de Arquer, R. Munir, A. H. Balawi, X. Lan, F. Fan, G. Walters, A. R. Kirmani, S. Hoogland, F. Laquai, A. Amassian, E. H. Sargent, *Nat. Mater.* **2016**, *16*, 258.
- [13] S. Wilken, J. Parisi, H. Borchert, *J. Phys. Chem. C* **2014**, *118*, 19672.
- [14] J. Choi, J. W. Jo, F. P. García de Arquer, Y.-B. B. Zhao, B. Sun, J. Kim, M.-J. Choi, S.-W. W. Baek, A. H. Proppe, A. Seifitokaldani, D.-H. H. Nam, P. Li, O. Ouellette, Y. Kim, O. Voznyy, S. Hoogland, S. O. Kelley, Z.-H. H. Lu, E. H. Sargent, *Adv. Mater.* **2018**, *30*, 1801720.
- [15] D. Egar, Y. Goldstein, A. Many, *RCA Rev.* **1975**, *36*, 508.
- [16] M. R. Lilliedal, A. J. Medford, M. v. Madsen, K. Norrman, F. C. Krebs, *Sol. Energy Mater. Sol. Cells* **2010**, *94*, 2018.
- [17] V. Lujala, J. Skarp, M. Tammenmaa, T. Suntola, *Appl. Surf. Sci.* **1994**, *34*, 82.
- [18] A. Wójcik, M. Godlewski, E. Guzewicz, R. Minikayev, W. Paszkowicz, A. Wójcik, M. Godlewski, E. Guzewicz, R. Minikayev, W. Paszkowicz, *JCrGr* **2008**, *310*, 284.
- [19] S. Y. Pung, K. L. Choy, X. Hou, C. Shan, *Nanotechnology* **2008**, *19*, 435609.
- [20] G. Konstantatos, E. H. Sargent, *Appl. Phys. Lett.* **2007**, *91*, 173505.
- [21] S. Pradhan, A. Stavrinadis, S. Gupta, Y. Bi, F. di Stasio, G. Konstantatos, *Small* **2017**, *13*, 1700598.
- [22] S. Pradhan, A. Stavrinadis, S. Gupta, S. Christodoulou, G. Konstantatos, *ACS Energy Lett.* **2017**, *2*, 1444.
- [23] F. Arca, S. F. Tedde, M. Sramek, J. Rauh, P. Lugli, O. Hayden, *Sci. Rep.* **2013**, *3*, 1324.
- [24] C. R. McNeill, I. Hwang, N. C. Greenham, *J. Appl. Phys.* **2009**, *106*, 024507.
- [25] V. Pecunia, Y. Yuan, J. Zhao, K. Xia, Y. Wang, S. Duhm, L. Portilla, F. Li, *Nano-Micro Lett.* **2020**, *12*, 27.
- [26] M. Li, G. Xing, L. F. N. A. Qune, G. Xing, T. Wu, C. H. Alfred Huan, X. Zhang, T. Chien Sum, *Phys. Chem. Chem. Phys.* **2012**, *14*, 3075.
- [27] H. K. Woo, M. S. Kang, T. Park, J. Bang, S. Jeon, W. S. Lee, J. Ahn, G. Cho, D. K. Ko, Y. Kim, D. H. Ha, S. J. Oh, *Nanoscale* **2019**, *11*, 17498.
- [28] M. Gabás, S. Gota, J. R. Ramos-Barrado, M. Sánchez, N. T. Barrett, J. Avila, M. Sacchi, *Appl. Phys. Lett.* **2005**, *86*, 042104.
- [29] Q. Xu, L. Meng, K. Sinha, F. I. Chowdhury, J. Hu, X. Wang, *ACS Photonics* **2020**, *7*, 1297.
- [30] K. Xu, X. Xiao, W. Zhou, X. Jiang, Q. Wei, H. Chen, Z. Deng, J. Huang, B. Chen, Z. Ning, *ACS Appl. Mater. Interfaces* **2020**, *12*, 15414.
- [31] X. Xiao, K. Xu, M. Yin, Y. Qiu, W. Zhou, L. Zheng, X. Cheng, Y. Yu, Z. Ning, *Appl. Phys. Lett.* **2020**, *116*, 101102.
- [32] C. Li, H. Wang, F. Wang, T. Li, M. Xu, H. Wang, Z. Wang, X. Zhan, W. Hu, L. Shen, *Light: Sci. Appl.* **2020**, *9*, 31.
- [33] J. Liu, H. Wen, L. Shen, *Nanotechnology* **2020**, *31*, 214001.
- [34] X. Geng, F. Wang, H. Tian, Q. Feng, H. Zhang, R. Liang, Y. Shen, Z. Ju, G. Y. Gou, N. Deng, Y. tao Li, J. Ren, D. Xie, Y. Yang, T. L. Ren, *ACS Nano* **2020**, *14*, 2860.
- [35] X. Chun, S. C. Cheng, X. Lin, V. P. Dravid, Y. W. Chung, Y. Zhu, J. P. Hare, C. L. Reeves, A. K. Cheetham, M. Rühle, H. W. Kroto, D. R. M. Walton, H. Chen, H. S. Yang, G. T. Wu, M. Wang, F. M. Deng, X. B. Zhang, J. C. Peng, W. Z. Li, B. A. Margaret Hines, G. D. Scholes, G. D. Scholes, M. A. Hines, *Adv. Mater.* **2003**, *15*, 1844.
- [36] K. Bertens, J. Z. Fan, M. Biondi, A. S. Rasouli, S. Lee, P. Li, B. Sun, S. Hoogland, F. P. García de Arquer, Z. H. Lu, E. H. Sargent, *ACS Mater. Lett.* **2020**, *2*, 1583.
- [37] I. Horcas, R. Fernández, J. M. Gómez-Rodríguez, J. Colchero, J. Gómez-Herrero, A. M. Baro, *Rev. Sci. Instrum.* **2007**, *78*, 013705.